

Article

In Situ Preparation of $\text{Pr}_{1-x}\text{Ca}_x\text{MnO}_3$ and $\text{La}_{1-x}\text{Sr}_x\text{MnO}_3$ Catalysts Surface for High-Resolution Environmental Transmission Electron Microscopy

Vladimir Roddatis * , Gaurav Lole and Christian Jooss *

Institute of Materials Physics, University of Goettingen, D-37077 Goettingen, Germany

* Correspondence: vroddatis@ump.gwdg.de (V.R.); cjooss@gwdg.de (C.J.);

Tel.: +49-551-39-25026 (V.R.); Tel.: +49-551-39-25303 (C.J.)

Received: 19 July 2019; Accepted: 29 August 2019; Published: 6 September 2019



Abstract: The study of changes in the atomic structure of a catalyst under chemical reaction conditions is extremely important for understanding the mechanism of their operation. For in situ environmental transmission electron microscopy (ETEM) studies, this requires preparation of electron transparent ultrathin TEM lamella without surface damage. Here, thin films of $\text{Pr}_{1-x}\text{Ca}_x\text{MnO}_3$ (PCMO, $x = 0.1, 0.33$) and $\text{La}_{1-x}\text{Sr}_x\text{MnO}_3$ (LSMO, $x = 0.4$) perovskites are used to demonstrate a cross-section specimen preparation method, comprised of two steps. The first step is based on optimized focused ion beam cutting procedures using a photoresist protection layer, finally being removed by plasma-etching. The second step is applicable for materials susceptible to surface amorphization, where in situ recrystallization back to perovskite structure is achieved by using electron beam driven chemistry in gases. This requires reduction of residual water vapor in a TEM column. Depending on the gas environment, long crystalline facets having different atomic terminations and Mn-valence state, can be prepared.

Keywords: perovskites; environmental transmission electron microscopy; surface chemistry

1. Introduction

Rational design of heterogeneous catalysts for high selectivity and turnover of chemical reactions requires detailed knowledge about the activity- and selectivity-determining structural properties, including catalytically active sites. Analysis of atomic and electronic structure of catalyst surfaces and subsurfaces under chemical reaction conditions thus is essential, since catalysts often undergo significant changes in surface and defect structure in their active state [1–3]. In situ atomic scale studies of electrocatalysts under working conditions can contribute substantially providing insights into the underlying reaction mechanism [4,5]. Environmental transmission electron microscopy (ETEM) offers unique opportunities in gaining atomic resolution images of surfaces and subsurfaces, formation of surface disorder, as well as spatially resolved spectroscopic information about the electronic structure and oxidation states of catalyst surfaces. In a dedicated ETEM instrument, a standard specimen chamber is replaced with a differently pumped environmental cell (E-cell) equipped with inlet and outlet lines [6]. The E-cell allows performing tomography [7], collecting high resolution images [8] and provides an easy access to use analytical techniques such as energy dispersive X-ray spectroscopy (EDX) and electron energy loss spectroscopy (EELS) [9,10], although the maximal pressure is limited to 20 mbar [11], or 100 mbar [12]. In its turn, dedicated gaseous holders [13] allow performing studies at pressures up to 4–5 bars [14], but field of view, spatial resolution, quality of images and use of analytical tools are limited because of silicon nitride membranes especially at low accelerating voltages [8]. Due to these recent technical improvements, ETEM has become a valuable instrument to reveal structural transformations of nanoparticles and catalyst surfaces in reactive environments [15–18].

At the same time, atomic resolution studies of catalysts require electron-transparent specimens with a thickness of only a few nanometers. Ideally, for reliable in situ experiments with cross-section specimens one needs to have an original surface of a catalyst showing no traces of preparation process in order to relate the obtained results with ex situ experiments. Conventional preparation methods include mechanical polishing and ion beam milling, where protection against surface damage is achieved by deposition of metal films [19]. In order to avoid sample thinning, Jacobs and Verhoefen [20] developed a method where a catalyst film is deposited onto a very thin Si_3N_4 membrane. Since the catalyst properties strongly depend on preparation methods and morphology, this method does not allow comparison with the properties of the system used in operando. Nowadays, focused ion beam (FIB) cutting combined with a lift-out technique is often applied for the preparation of ultrathin lamellas of almost any kind of material [21]. This also allows integration of lamella onto micro-electro-mechanical systems (MEMS) used in dedicated in situ holders. In order to minimize ion beam damages, the presence of protection layers such as Pt/C or W/C films is required [22]. However, both metals form clusters and can be very active as catalysts, thus masking the activity of studied material. Moreover, the presence of heavy atoms can change the contrast of high-resolution images collected to observe dynamical changes of catalysts surface. Alternative protection layers containing mainly carbon have been also reported [23].

Recently, it was demonstrated that electron beam driven epitaxial recrystallization of an amorphous surface layer developed during FIB cutting on the preexisting crystalline SrTiO_3 is possible with high beam currents in scanning TEM (STEM) mode [24]. However, in high vacuum the resulting oxygen stoichiometry cannot be controlled. In a gaseous environment, the effects caused by the interaction of electron beam with the sample can be combined with a control of chemical changes. For example, STEM EELS imaging of a manganite in 3 mbar of O_2 can give rise to sample oxidation by oxygen uptake [25]. This is in contrast to reduction of the same material in high vacuum at the same used electron fluxes due to oxygen knock out.

In this study, we demonstrate a FIB based two-step preparation method of cross-section TEM perovskite oxide specimens, resulting to well-ordered crystalline surface edges with controlled oxygen stoichiometry and avoiding any contamination by metallic impurities. We have selected (001) oriented epitaxial $\text{La}_{1-x}\text{Sr}_x\text{MnO}_3$ (LSMO) with $x = 0.4$ and $\text{Pr}_{1-x}\text{Ca}_x\text{MnO}_3$ (PCMO) with $x = 0.1$ and 0.33 thin films showing quite high activity as catalyst materials for the oxygen evolution reaction [17,26–28]. The first essential step for the lamella preparation is the FIB cutting using a protection layer of alkali resistant positive photoresist. After ion milling and removal of the photoresist by plasma etching thin amorphous layers still can present on materials. The second step is the in situ recrystallization of remaining amorphous surface layers. Epitaxial recrystallization can be achieved in O_2 as well as in He and N_2 with residual O_2 , leading to different surface terminations. The partial pressure of residual water in the column of electron microscope is found to be an essential parameter determining whether the epitaxial recrystallization of the perovskite or phase decomposition into a binary oxide evolves. Since the selected materials have significantly different electrical properties we think that observed effects are valid for many other complex oxides as well.

2. Results

The low magnification cross-section image of LSMO ($x = 0.4$) specimen prepared using photoresist protection layer is shown in Figure 1a. Two windows of different thickness are used to demonstrate the opportunity to control the thickness of lamella. The HRTEM image in Figure 1b and HRSTEM image in Figure 1c show that plasma cleaning during 5 min removes the rest of the photoresist completely.

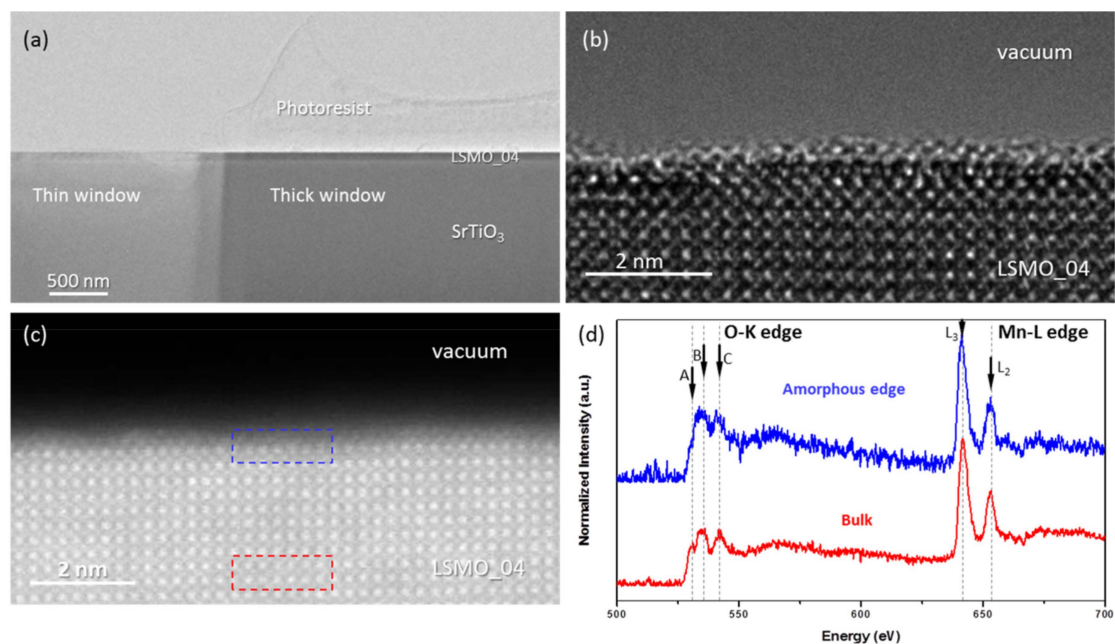


Figure 1. (a) Low magnification image of $\text{La}_{0.6}\text{Sr}_{0.4}\text{MnO}_3$ (LSMO) ($x = 0.4$) lamella prepared with the use of photoresist protection layer; (b) High-resolution transmission electron microscope (HRTEM) image of an edge collected from the thin window area; (c) high-resolution scanning TEM (HRSTEM) image, the areas marked with red and blue are used to collect electron energy loss spectroscopy (EELS) data (0.1 eV/channel) presented in (d). Spectral features marked with A, B, C, L_2 and L_3 are discussed in text.

Both the HRTEM and HRSTEM images show that the $\sim 40\text{--}50$ nm thin lamella has a crystalline structure, despite a thin subunit-cell thick disordered surface layer. EELS spectra presented in Figure 1d show that this disordered surface of LSMO film has lower oxidation state of Mn than the bulk. Three characteristic peaks of O K-edge are visible at 529 eV (A), 534 eV (B) and 543 eV (C). The prepeak (A) due to O 1s transitions to O 2p states hybridized with Mn 3d. It reflects the presence of O 2p holes. The other two peaks are due to transition from O 1s into O states which are hybridized with Ca d / Pr d states (B) and free electron like features (C) [29]. Since oxygen vacancies are electron donors, a decrease in the intensity of the prepeak A indicates an increasing amount of oxygen vacancies. Its lack in the spectrum from the surface points to a reduced state of Mn. This is also confirmed by the analysis of the Mn L-edge. The Mn L edge is due to transition of the spin-orbit split 2p into Mn 3d states and thus shows L_3 and L_2 subfeatures. The L_3/L_2 intensity ratio is a measure of the Mn oxidation state [30]. Our analysis yields an oxidation state between +2.6 and +2.8 for the amorphous material. Atomic force microscopy images of the same LSMO 0.4 films show crystalline surface which consist of atomically flat terraces and unit cell height steps [28] as a result of step flow growth mode on vicinal SrTiO_3 (STO) (001). There is some evidence that crystalline LSMO films on SrTiO_3 can have reduced surfaces after vacuum annealing [31]. Since the LSMO films studied here are annealed in oxygen after growth, complete oxidation of the surface as seen in [31] is expected. We thus attribute surface disorder and Mn reduction of the TEM lamella shown in Figure 1 to preparation-induced damage. Indeed, scattering of Ga ions during FIB thinning can give rise to preferential knock out of oxygen at the LSMO-photoresist interface.

The possibility of a beam stimulated transformation of preparation induced surface disorder to the perovskite crystal structure is demonstrated for a 2–3 nm thick amorphous PCMO layer on top of crystalline PCMO $x = 0.33$ in different gases, i.e. He, N_2 , and O_2 in Figure 2. The cross-section lamellas have been cut from the PCMO/LSMO/Nb-STO stack; 300 kV electron beam stimulation is performed in TEM mode with a beam of about 100 nm in diameter and ~ 4 nA current. Such illumination conditions result in a $14,000\text{--}20,000$ $\text{e}^- \cdot \text{s}^{-1} \cdot \text{\AA}^{-2}$ dose rate. The process takes about 20–25 min in order to complete

the transformation of the amorphous layers in He (Figure 2a) or in N₂ (Figure 2c) to a surface facets having of a length of about a few dozen nanometers, Figure 2b,d, respectively. It is noteworthy that the first facets of several nanometers in length were formed already after the first three minutes. The corresponding movies S1, S2 and S3 show the real time changes of structure in N₂ gas ($p_{N_2} = 5$ ubar) at the beginning, after about 20 min and at the end of process, respectively. During all stages of process a pronounced atomic dynamics at the surface is observed similar to Epicier et al. [32]. Also, Figure 2b,d demonstrate that electron beam irradiation can result in different surface terminations. This will be discussed in detail further down. Thus, the process resembles the so-called solid phase epitaxial (SPE) growth, where an initially amorphous Si [33] or complex oxide [34] thin film is epitaxially recrystallized on a crystalline template at elevated temperatures. Remarkably, the electron-beam-induced SPE process in our environmental TEM study is observed at room temperature and depends on a reactive gas environment. The required electron flux is orders of magnitude lower than that reported for the transformation of amorphous STO into perovskite structure during operation the microscope in STEM mode (electron dose rate $\approx 1 \times 10^8 \text{ e}^- \cdot \text{s}^{-1} \cdot \text{\AA}^{-2}$, high vacuum conditions $p = 10^{-7}$ mbar) [24].

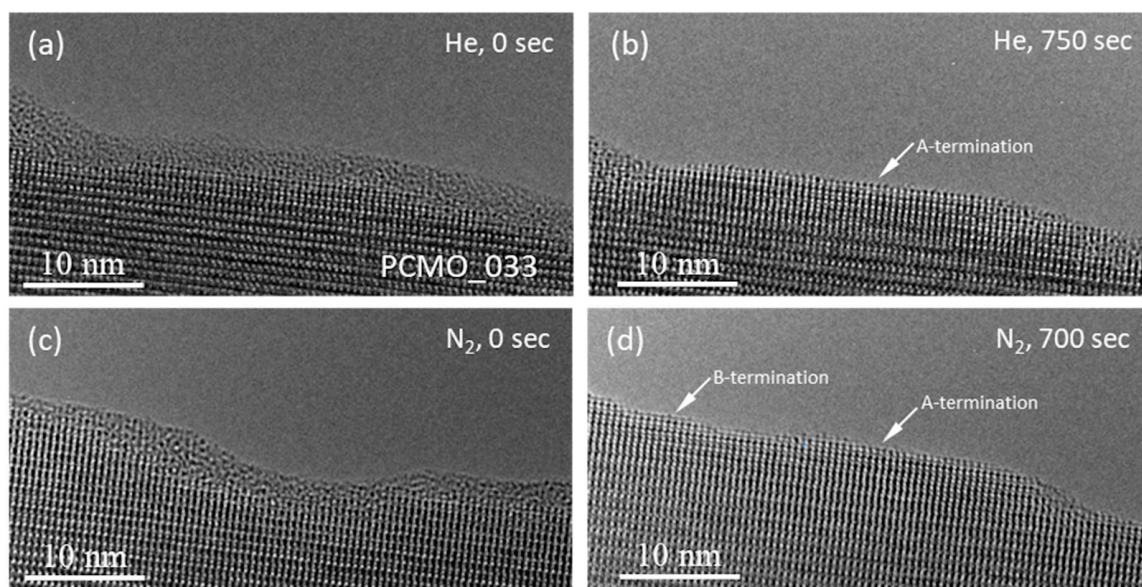


Figure 2. HRTEM images of an edge of Pr_{1-x}Ca_xMnO₃ (PCMO) ($x = 0.33$) material in He ($p_{He} = 50$ ubar) at the beginning (a), after 750 s (b), and in N₂ at the beginning (c) and after 700 s (d), respectively.

The crystallization in O₂ gas proceeds similarly as in He or N₂, however, it takes only about 5–6 min at the same illumination conditions. Snapshots of crystallization in O₂ are presented in Figure 3. At the beginning, during several minutes, only mobility of atoms in amorphous layer is visible, similar to observations in He or N₂ (Figure 3a–d). Then, the growth of small pyramidal islands is observed (one island is marked with the yellow arrow). These islands grow slowly and over time reach the surface of amorphous layer (Figure 3e). At the same time the thickness of amorphous layer is decreasing. Finally, the amorphous material between crystalline islands also becomes crystalline, and flat facets up to 10 nm in length are formed (Figure 3f–h). It is important to note that in all gases (He, N₂ and O₂), the final phase of crystallization, i.e. when crystalline islands have sprouted through the amorphous layer, proceeds faster.

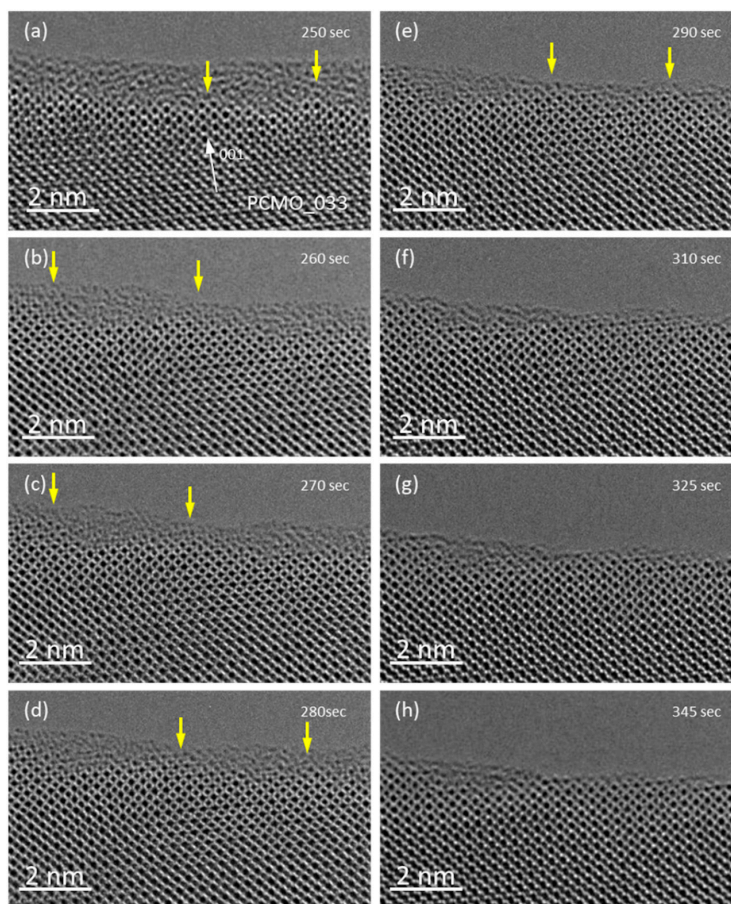


Figure 3. A series of images showing transformation of amorphous edge of PCMO ($x = 0.33$) into crystalline structure. The images were collected in O_2 , $p_{O_2} = 50$ ubar. (a) During several minutes only mobility of atoms in amorphous layer is visible. (b–d) The growth of small island of pyramidal shape is observed (the place is marked with the yellow arrow). (e) These pyramids grow slowly and reach the surface of amorphous layer. Its thickness becomes smaller at the same time. Finally, amorphous areas between pyramids also transform in crystalline perovskite oxide phase, and flat facets up to 10 nm in length are formed (f–h).

In order to verify the chemical composition of original, amorphous and recrystallized PCMO, the EELS spectra were collected at the beginning of experiment and after the recrystallization was completed. In addition, K- edges of oxygen and L-edges of Mn were collected with the better energy resolution to examine the oxidation state of Mn.

The HRSTEM images shown in Figure 4a,b demonstrate an edge of PCMO ($x = 0.33$) film before and after recrystallization in oxygen at $p_{O_2} = 50$ ubar, respectively. Clean and atomically sharp steps having a height of few unit cells are commonly observed. The corresponding EELS spectra are shown in Figure 4c. All spectra were aligned using a zero-loss peak (ZLP) as a reference, and then normalized. Note, that the spectrum collected from the amorphous edge looks noisier than other spectra because of smaller thickness of the edge. Based on the reduced intensity of the O K prepeak (A), the crystallization in He results in a reduced state of Mn at the surface. The analysis of L_3/L_2 ratio of Mn L-edge yields an average value of 3.30 ± 0.06 and a value of 3.24 ± 0.02 close to the surface (see Figure S1). In contrast, when the crystallization was performed in O_2 the average value of the Mn oxidation state is 3.36 ± 0.06 and 3.35 ± 0.06 at the surface (see Figure S2). All values are close to the value for the nominal composition as in bulk (+3.33). Thus, the use of oxygen leads to the epitaxial recrystallization of a stoichiometric PCMO, whereas in He, a crystalline edge with increased lattice disorder is developed. The average Mn valence state is the same in He as in O_2 within error based on the analysis of the

L_3/L_2 intensity ratio. However, there is a strong reduction of the O K prepeak at the surface, pointing towards a more reduced state in He. The effect of disorder on electronic properties is quite complex. For example, in addition to oxygen vacancies, charge neutral pair defects can contribute to the lattice disorder in He which can maintain the Mn valence while changing the O K edge. Nevertheless, for all three gases used, the lattice spacing up to most top unit cell corresponds to the bulk PCMO material within error.

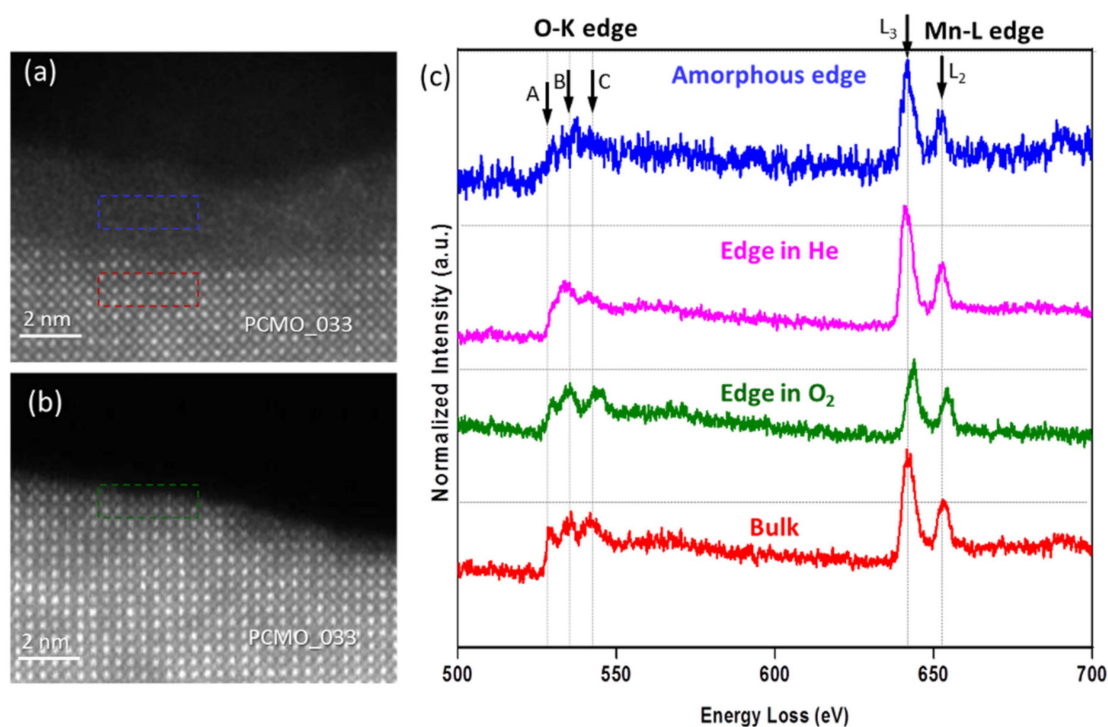


Figure 4. HRSTEM images of PCMO ($x = 0.33$) before (a) and after (b) crystallization under electron beam in oxygen, respectively. (c) EELS spectra (0.1 eV/channel) collected from the areas marked with different colors in (a) and (b). Spectral features marked with A, B, C, L_2 and L_3 are discussed in the text.

The chemical composition of the amorphous layer as well as recrystallized material was also verified using EELS, and only Pr, Ca, Mn, and O edges were detected; Figure 5 shows the results for the PCMO, $x = 0.33$. A HRSTEM image of the recrystallized area is shown in Figure 5a. The EELS spectra reveal a decrease of Ca content in the surface unit cells (Figure 5b). Since the properties of perovskite materials strongly depend on the amount of doping, a careful choice of the illumination conditions and the environment is very essential for control of the chemical composition of the recrystallized perovskite. A long lasting electron beam illumination to fully recrystallize the amorphous layer obviously results in element-specific knock out damage of light elements which is evidenced by chemical analysis (Figure 5). In addition, the lattice disorder of the recrystallized perovskite due to off-stoichiometry is visible by broadening of spots and changing of their intensities in corresponding FFT images calculated from the HRTEM images collected in all the gases used. The effect is notably less pronounced in series of HRTEM images collected from the same TEM lamella in O_2 (see Figures S3 and S4), supporting our statement of a less vacancy disordered structure because Mn acquires its nominal valence state.

As it was already described above, that flat facets were formed from the amorphous material at the surface of PCMO in all He, N_2 and O_2 gases used. Moreover, a careful inspection of the top atomic layer revealed that the termination of the recrystallized edge depends on the gas used. This effect is shown in Figure 6. Both A- and B-cation stable terminations were observed after recrystallization in N_2 (Figure 6a), while only the A-cation termination of facets was found after recrystallization in He (Figure 6d). The observation is verified by HRTEM image simulations presented in Figure 6b,c,e,f, respectively. The HRTEM images of PCMO along [100] and [010] look differently because of the

symmetry inherent in the Pbnm space group. The Mn-O (B-termination along [010]) is obviously recognized in Figure 6a,b because of a characteristic zigzag motif of Mn-O atomic columns (see Figure S6 for details). In the case of A-termination the difference in HRTEM images along [100] and [010] is almost invisible.

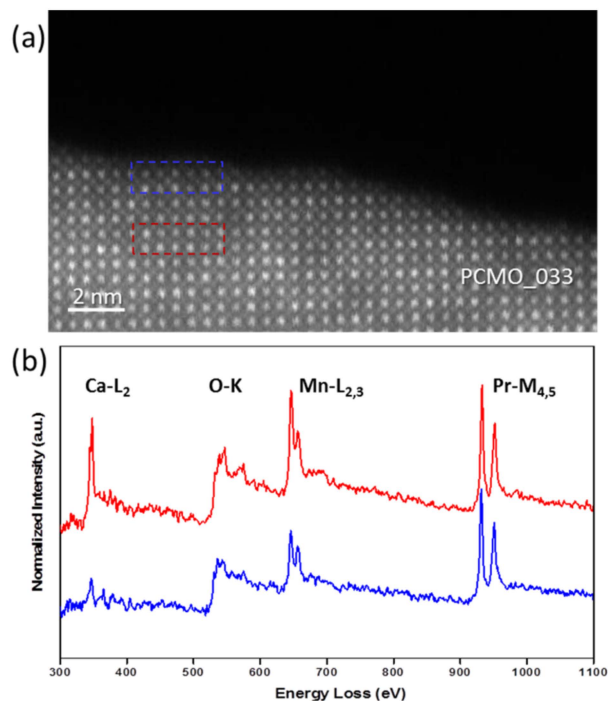


Figure 5. (a) HRSTEM image of PCMO ($x = 0.33$) with two selected area used to verify the chemical composition of original PCMO material and recrystallized amorphous layer. The corresponding normalized spectra (1 eV/channel) are shown in (b), and the signal from Ca is remarkably weaker at the last unit cell.

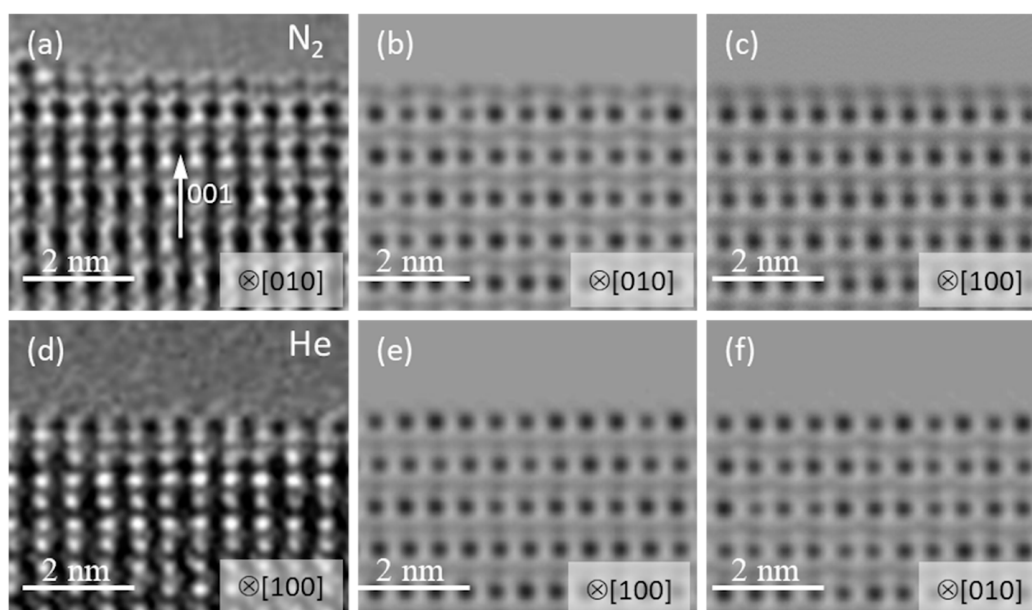


Figure 6. Experimental HRTEM images of PCMO ($x = 0.33$) collected in N_2 (a) and in He (d) at $p = 50$ ubar; (b,c,e,f) corresponding calculated images along [100] and [010] directions. Both A- and B-cation stable terminations are visible in N_2 , whereas only the A-cation termination of facets is visible in He.

As an example for the recrystallization of PCMO ($x = 0.1$), Figure 7a–c shows the evolution in He. The first crystalline facets showed up only after 28 min, compared with about 11 min for PCMO ($x = 0.33$). After such a long irradiation time, one can expect a high density of defects in the material. Indeed, the spots in the FFT image became more smeared after 28 min, which is evidence of the increased structural disorder (see Figure S5). The weak signal of Ca is still visible in the EELS spectra taken from the edge (Figure 7d,e) taking into account that the concentration of Ca is already very low in the original material. In general, the EELS data from PCMO ($x = 0.1$) sample are very scattered. In some areas the analysis of O-K and Mn-L edges shows that the oxidation state of Mn is in the +3.0–+3.3 range (Figure 7f) pointing against a large concentration of single oxygen vacancies as origin of the lattice disorder. However, very low values of the oxidation state of Mn were also observed (Figure S7).

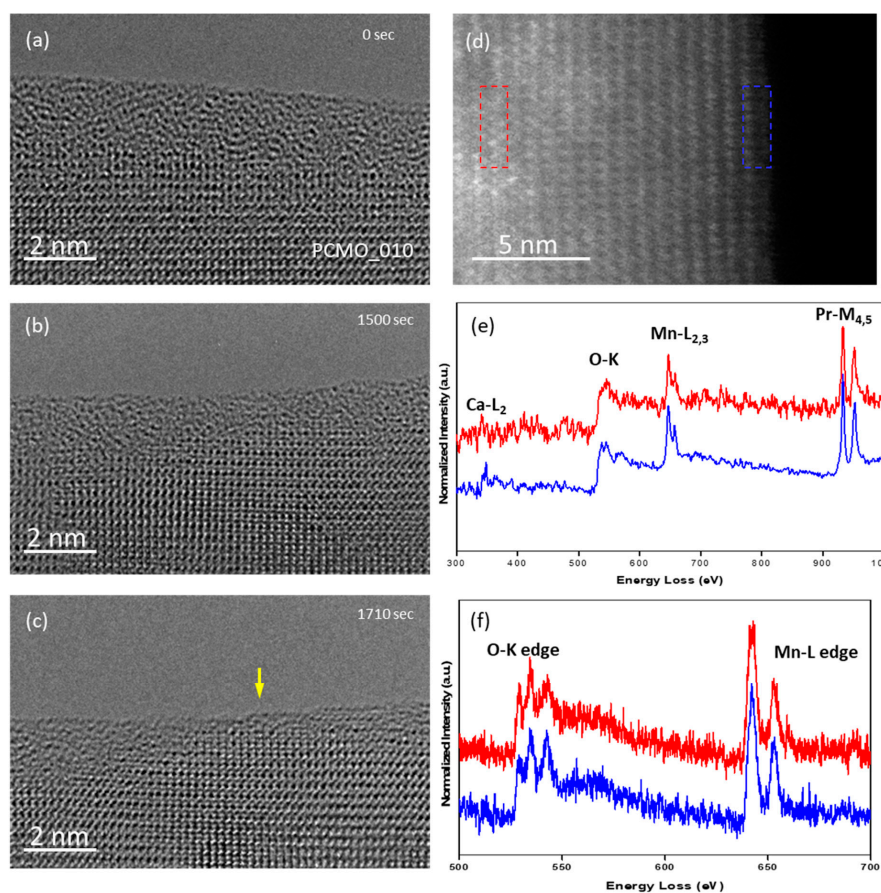


Figure 7. (a)–(c) HRTEM images showing transformation of amorphous edge into crystalline for the PCMO ($x = 0.1$) in He gas at pressure of 50 ubar. The first crystalline facets (marked with the yellow arrow in b) start to appear after ~28 min (1710 s). (d) High-angle annular dark field (HAADF) image of the recrystallized area. (e) EELS spectra (1 eV/channel) demonstrate the presence of Pr, Ca, Mn and O. (f) EELS spectra (0.1 eV/channel) reveal a slightly reduced Mn oxidation state.

Usually, the recrystallization of the edge in PCMO ($x = 0.1$) took much longer for all gases used. This is however consistent with cyclic voltammetry studies, showing a pronounced surface $\text{Mn}^{2+}/\frac{1}{2}\text{V}_\text{O} \leftrightarrow \text{Mn}^{3+}/\text{O}_\text{O}$ redox couple for PCMO (0.33) which is absent in $x = 0.1$. As an example, Figure 8 shows cyclic voltammograms of two epitaxial (001) oriented PCMO ($x = 0.1$ and $x = 0.33$) films on LSMO/Nb:STO at pH = 13 measured at a sweep rate of 10 mV/s. The electrochemical measurements were performed in 0.1 M potassium hydroxide (KOH) electrolyte prepared by diluting KOH stock solution with deionized water (for neutral pH see [17]). Both films show an exponential increase of currents at positive potential due to oxygen evolution reaction (OER), as verified by measuring the formed O_2 by a ring electrode. The pronounced redox peak for $x = 0.33$ indicates an easier oxygen vacancy formation and healing

process compared to $x = 0.1$ which explains the observation of faster epitaxial recrystallization for $x = 0.33$ compared to $x = 0.1$ in the ETEM experiments.

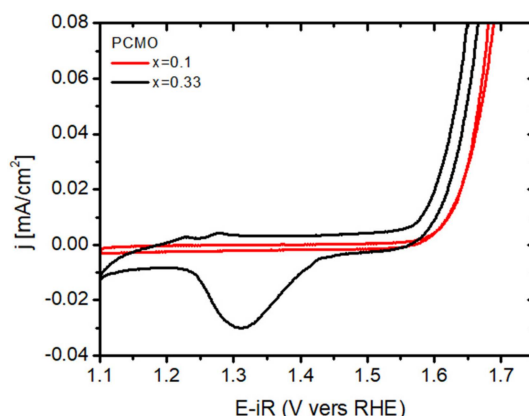


Figure 8. Cyclic voltammograms of (001) oriented PCMO ($x = 0.1$) and ($x = 0.33$) films in 0.1 M KOH. The $x = 0.33$ film shows a redox couple which is overlapping to the onset of OER at the anodic branch and well separated from OER at the cathodic branch. This redox couple is absent for PCMO ($x = 0.1$).

Finally, we note that the epitaxial crystallization only happens at the preexisting crystalline interface, when the partial water pressure is $p_{\text{H}_2\text{O}} < 5 \cdot 10^{-8}$ bar (Figure 9). In other words, the residual pressure of water vapor in the column should be below 0.1% of the working gas. Exemplary snap shot from the Quadera™ software (Figure 9a) shows two periods during the experiment in He when the cold trap was not used (Cold trap OFF) and after it was activated (Cold trap ON). At the higher pressure of water vapor ($p_{\text{H}_2\text{O}} = 25 \cdot 10^{-8}$ bar, Cold Trap OFF) the amorphous layer was transformed into randomly oriented PrO_2 particles as shown in Figure 9b (see also Figure S8). Similar structural transformations of initially amorphous areas were reported earlier for the ETEM experiments performed in water vapor at higher pressures of $5 \cdot 10^{-6}$ and $5 \cdot 10^{-5}$ bar [18], and this is consistent with the drop of OER activity in electrochemical experiments over time due to Mn leaching into the electrolyte [28]. After the cold trap was filled with liquid nitrogen and as soon as the partial pressure of water vapor dropped about an order of magnitude ($p_{\text{H}_2\text{O}} = 25 \cdot 10^{-9}$ bar), the epitaxial recrystallization was observed (Figure 9c) similar to results presented in Figures 2–4.

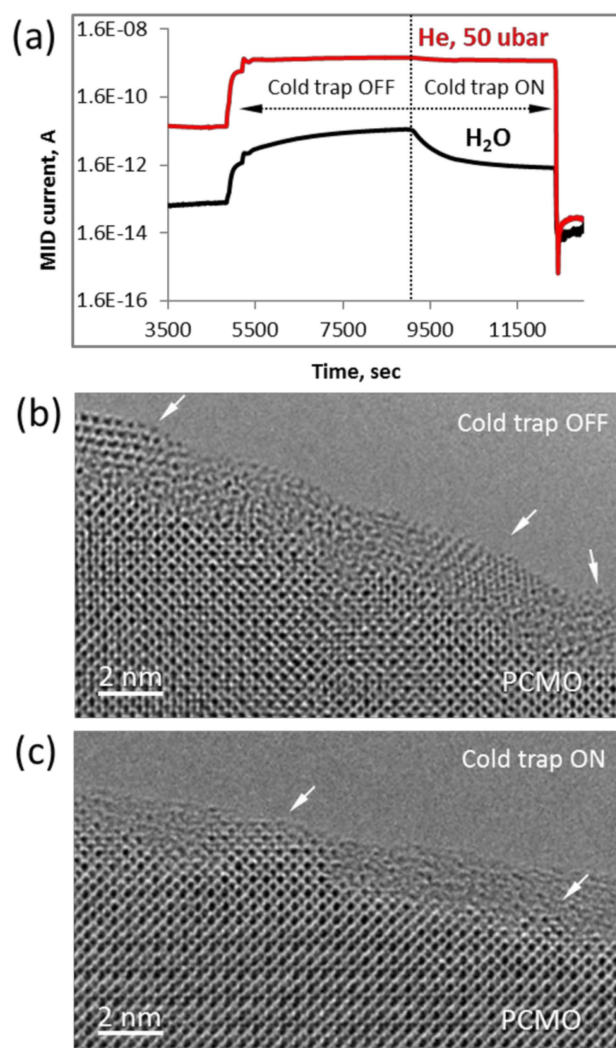


Figure 9. (a) A snapshot of Quadera™ software during environmental transmission electron microscopy (ETEM) experiment at 50 ubars of He with and without activated cold trap. Experimental HRTEM images in He when the cold trap was OFF and ON are shown in (b) and (c), respectively. The white arrows point out on randomly oriented PrO₂ particles, growing in amorphous layer (b), and epitaxially growing pyramids of PCMO ($x = 0.33$) (c).

3. Discussion

As already mentioned, the observed recrystallization of amorphous PCMO resembles SPE of an amorphous Si which happens via a moving amorphous/crystalline interface, where velocities of a few nm per min requires elevated temperatures above 500 °C [33]. The recrystallization temperature can be significantly reduced to around 200–300 °C, if the recrystallization is assisted by ion irradiation [34]. Although the electron-beam induced recrystallization reported here also happens via the movement of the crystalline/amorphous interface, it however strongly differs from the SPE. First of all, the beam induced temperature increase ΔT in the TEM lamella is irrelevant, excluding a thermally activated growth mechanisms. The upper limit of temperature increase for the used beam parameters is $\Delta T = 0.015$ K (see Appendix A). Furthermore, the epitaxial recrystallization in our experiments strongly depends on the gas environment. In high vacuum conditions, no epitaxial growth is observed. Here, the amorphous layer partially disappears on timescales of tens of minutes due to electron beam-induced sputtering of atoms from damaged areas.

In oxygen both amorphous PCMO $x = 0.1$ and $x = 0.33$ layers transform into a crystalline perovskite layer under oxygen uptake during the recrystallization process. This is confirmed by a change of

the Mn valence state from about +2.9 in the amorphous to close to the nominal value. There are three possible candidates for beam induced electronic excitations driven the observed solid state chemistry: (i) a photo-chemical process driven by beam induced generation of hole carriers. Since the lifetime of photo-holes (1 ns) is orders of magnitudes below the recrystallization rate (1 s per atom), a photo-chemical process is highly improbable. (ii) An electrochemical process driven by beam induced positive electric potentials due to secondary electron emission. Such an electrochemical mechanism is feasible: The relevant redox potential for oxygen in manganites is of the order of 1 V (see Figure 8), a potential which can be easily generated in semiconductors at dose rates above $10.000 \text{ e}/\text{\AA}^2\text{s}$ [35]. (iii) Radiolysis, the dissociation of molecules or covalently bound solids by inelastic scattering of primary electrons with bond forming valence electrons. Whereas radiolysis may be relevant for the dissociation of molecular oxygen and activation of O_2 for the solid state reaction, it is irrelevant in ionic or metallic solids. Here, this is confirmed by the formation of rather perfect crystalline perovskite structure in O_2 .

Beam-induced displacements of atoms by nuclear collisions is probable process for activating the growth of crystalline PCMO by a moving amorphous/crystalline interface as observed in O_2 as well as in the inert gases N_2 and He. However, it cannot explain the oxygen uptake in O_2 . Maximum energy transfer takes place by backscattering of electron which could displace surface adsorbed oxygen into the amorphous material on the top side of the lamella, but would lead to sputtering on the bottom side and at the edge. This would represent an “inverse sputtering process”, where in contrast to HV, oxygen vacancies are filled by activated surface oxygen. Conversely, in N_2 , one should then form oxynitrates, in contrast to observation.

The observation that the amorphous phase transforms into crystalline PrO_x nanoparticles in the presence of sufficient partial pressure of H_2O by preferential leaching of Mn and also Ca give strong hints about the beam induced chemistry involved. Based on the equation provided by Egerton et al. [36], for the energy transfer between a high energy electron and an atom due to elastic scattering, we calculate the upper limit for the different atomic species: E_{max} is 53.1 eV (O_2), 42.5 eV (Ca), 34.0 eV (Mn) and 14.4 eV (Pr). This must be compared to binding energies of $E_b = 50 \text{ eV}$ (O), 70 eV (A site) [14] and between 50–170 eV (Ti as an exemplary B-site in BaTiO_3) [37], depending on the crystal orientation of a perfect perovskite single crystal. This is consistent to the statement that $E_{max} < E_b$. However, E_b should be generally reduced in the amorphous phase of the same chemical elements, because of the lower density of packing, open voids and change of bond coordination. Remarkably, our experiments show that the preferential sputtering of atomic species strongly depends on the gas environment. In HV, the amorphous surface layer is partially removed with preferential sputtering of O, Ca and Mn without formation of PrO_x . In contrast, in O_2 or inert gases, the presence/absence of preferential leaching of Mn and Ca strongly depends on the $p_{\text{H}_2\text{O}}$. This reflects that the vacancy formation energy close to surfaces depends on the surface chemistry. The presence of adsorbed surface H_2O , where Mn^{2+} and Ca^{2+} is soluble, clearly facilitates the leaching of displaced Mn and Ca species, giving rise to the formation of PrO_x . In contrast, in O_2 this process is suppressed and the uptake of oxygen for example by occupation of V_O vacancy sites is the dominating process.

Clearly, the crystallization rate and thus the velocity of the amorphous/crystalline interface is slowed down in inert gases He and N_2 , compared to experiments in O_2 . This indicates, that beam induced atomic displacements cannot be the only driving force for the movement of the interface. Figure S9 shows that residual molecular and atomic oxygen is also present in an inert gas experiment, e.g., in He. Its relative concentration is only slightly reduced after switching on the cold trap. The epitaxial recrystallization in inert gases may thus be influenced by the presence of oxygen. The analysis of the Mn valence state after He in comparison with the amorphous material at the pristine lamellas does not provide evidence for a large amount of oxygen uptake, since the Mn valence state is the same within error. However, sputtering of oxygen may be still compensated by the electrochemical oxidation, which is slowed down at lower p_{O_2} . This could indicate that beam induced epitaxial recrystallization in inert gases is also accompanied by a solid state chemical reaction with oxygen.

Consequently, even without net uptake of oxygen, the presence of surface adsorbed oxygen species can alter the beam induced effects from absent in high vacuum, over leaching in H₂O to perovskite epitaxy in inert gases.

4. Materials and Methods

Thin films of Pr_{1-x}Ca_xMnO₃ (PCMO) with different Pr/Ca ratio ($x = 0.1$ and $x = 0.33$) were grown on Nb-doped SrTiO₃ (001) with a 20 nm thick epitaxial La_{0.6}Sr_{0.4}MnO₃ (LSMO) (001) interlayer by reactive Xe-ion beam sputtering in an oxygen atmosphere with a partial pressure of $1.4 \cdot 10^{-4}$ mbar at the deposition temperature of $T_{\text{dep}} = 1020$ K. The PCMO film of thickness of $d \approx 100$ nm reveals epitaxial growth with [001]/[110] growth domains, inevitably present due to twinning. The LSMO interlayer was grown in order to adjust the lattice misfit between STO and PCMO. The growth parameters and detailed structural characterization of studied films is published elsewhere [17,18,28].

Specimens for in situ TEM studies were prepared by lift-out technique using a NanoLab 600 (Thermo Scientific™, former FEI, Hillsboro, Oregon, USA) dual beam instrument operated at 30 and 5 kV. Conventional method with FIB lift-out technique usually starts from the deposition of platinum/carbon (Pt/C) protection layers by electron or ion beam [38]. Since Pt is highly active catalyst, its presence at the surface of perovskites should be excluded. All lamellas in this study were prepared using a protection layer of Alkali Resistant Positive Photoresist X AR-P 5900/4 (ALLRESIST GmbH, Strausberg, Germany) which was deposited onto the surface of LSMO and PCMO thin films before FIB cutting procedure. Electron transparent lamella was finally cleaned with Ar⁺ ions with energies from 500 eV to 100 eV using a Gatan PIPS 691 ion polishing system. The rest of protection layer was removed with a plasma cleaner prior TEM studies. High-resolution TEM (HRTEM), electron diffraction (ED) and STEM studies were performed using an aberration corrected Titan 80-300 environmental microscope (Thermo Scientific™, former FEI, Hillsboro, Oregon, USA) operated at 300 kV. The specimens were imaged along [010] and [110] crystallographic directions in the Pbnm space group. ETEM experiments are performed with N₂, He, O₂ gases. The chemical composition of gas environment was controlled by the Residual Gas Analyzer (RGA) QMG220 (Pfeiffer Vacuum GmbH, Germany) controlled by Quadera™ software (version 4.3, INFICON Aktiengesellschaft, Liechtenstein, 2010). During the experiments the deviations of pressure from desired values of 5 and 50 microbars did not exceed 5%. Other residual gases are always present in the inlet tubes and electron microscope column. In order to minimize their influence the inlet tubes were purged firstly with the working gas. Then, the specimen chamber was also purged with the working gas during at least half an hour, and the electron beam was blanked. These procedures allowed reducing the presence of other gases to be less than 1%. For example, during the used experimental setting, typical values are H₂O: 1% (cold trap off) and 0.05% (cold trap on); O₂: 0.2%; N₂: 0.04%; hydrocarbons (unspecified) and very low amounts of atomic nitrogen and oxygen. Switching on the cold trap thus changes the main residual gas impurity from H₂O to O₂ (see S11). EELS data were collected with a Gatan Imaging Filter (GIF) Quantum 965ER (Gatan, Pleasanton, CA, USA). Atomic models were built using the Vesta software package (version 3.4.7, 2019) [39]. High-angle annular dark field (HAADF) contrast and spectrum imaging was used in order to visualize change in chemical composition. HRTEM images were simulated using QSTEM software (version 2.51, 2019) [40].

5. Conclusions

We successfully demonstrated high-quality preparation of cross-section TEM lamella of complex oxide thin films by FIB, using metal free protection layer, i.e. photoresist. Although beam damage is small, subunit cell disordered layers remain on the surface after plasma etching of photoresist which can be treated in situ by beam driven recrystallization in suitable gas environments. It allows the formation of well-ordered crystalline facets with different surface termination, dependent on the gas. This is an important prerequisite for the in situ atomic scale observation of active states of catalysts. The work also demonstrates the feasibility of direct imaging of solid state chemical and structural

transformations from amorphous to crystalline structures on atomic scale. The length of modified edge at TEM lamella varies in a range from several nanometers to several tens or even hundred nanometers. The chemical composition of the modified area depends on the gases used, as well as on the presence of residual water molecules in the column of electron microscope. The presence of water can cause selective leaching of atomic species (Mn and Ca) and thus irreversible chemical changes of surface of PCMO perovskites. By contrast, the reduction of water partial pressure below $5 \cdot 10^{-8}$ bar forms conditions, where crystalline perovskite oxide structure can be grown from a damaged amorphous material by electron-beam-induced solid phase epitaxy controlled by gas regulated solid state chemistry. The observation that the nominal Mn oxidation state can be reached from the reduced amorphous state in $p_{O_2} = 50 \cdot 10^{-6}$ bar points to the key role of residual oxygen in N_2 and He environments for the healing of preparation induced damage. At this point of our studies, we suggest that beam-induced atomic displacements drive the crystallization front between the amorphous and crystalline phase. However, this process is most probably accompanied by beam-induced electrochemical oxidation which compensates the sputtering of oxygen or can even drive oxygen uptake to the stoichiometric level. This statement is strongly supported by the observed higher speed of epitaxial recrystallization for the material with a pronounced electrochemical redox couple $Mn^{2+}/\frac{1}{2}V_O \leftrightarrow Mn^{3+}/O_O$.

The reported results are important both for the design of in situ experiments related to the study of heterogeneous catalysis and battery technology in oxide-based materials. The well controlled design of perovskite oxide surface edges in O_2 and inert gases at low p_{H_2O} is a vital requirement for the realization of a well-defined starting state of the surface in situ reactions. In order to have better control over size and chemical composition of the modified area, significant improvements of specimen stage stability, inlet and outlet systems of ETEM as well as chemical analysis of gaseous environment is highly desirable.

Supplementary Materials: The following are available online at <http://www.mdpi.com/2073-4344/9/9/751/s1>: Figure S1: The PCMO ($x = 0.33$) after electron beam treatment in He at 50 μ bars, Figure S2: The PCMO ($x = 0.33$) after electron beam treatment in O_2 at 50 μ bars, Figure S3: HRTEM image and rotationally averaged profiles of PCMO in O_2 and in He ($x = 0.33$), Figure S4: HRTEM image and rotationally averaged profiles of PCMO in He ($x = 0.1$), Figure S5: Analysis of broadening of spots in FFTs, lattice disorder in PCMO ($x = 0.1$), Figure S6: (1) Through focus series of HRTEM images of PCMO ($x = 0.33$) for the thickness of 10 nm, (2) Experimental and calculated HRTEM images of PCMO ($x = 0.33$) for the thickness of 3 nm, Figure S7: The PCMO ($x = 0.1$) after electron beam treatment in He at 50 μ bars, Figure S8: HRSTEM image and EELS spectrum of PrOx particle at the surface of PCMO ($x = 0.33$), Figure S9: An example of multiple ion detection scan in Quadera™ software, Table S1: Summary of the Mn valence PCMO ($x = 0.33$) after electron beam treatment in He at 50 μ bars, Table S2: Summary of the Mn valence of PCMO ($x = 0.33$) after electron beam treatment in O_2 at 50 μ bars. Table S3 (1): Simulation parameters for the through focus series, (2) Simulation parameters for individual experimental images, Table S4: Summary of the Mn valence of PCMO ($x = 0.1$) after electron beam treatment in He at 50 μ bars.

Author Contributions: Conceptualization: C.J. and V.R.; Formal analysis: G.L. and V.R.; Investigation: G.L. and V.R.; Resources: C.J.; Writing—original draft preparation: V.R.; Writing—review and editing: V.R., G.L. and C.J.; Visualization: V.R. and G.L.; Supervision: C.J. and V.R.; Project administration: C.J. and V.R.; Funding acquisition: C.J. and V.R.

Funding: The authors are grateful for financial support by the Deutsche Forschungsgemeinschaft, grant number CRC 1073 (Projects C02 and Z02).

Acknowledgments: The authors wish to thank V. Radisch, V. Moshnyaga and V. Bruchmann-Bamberg for excellent support in TEM specimen preparation.

Conflicts of Interest: The authors declare no conflict of interest.

Appendix A

We calculate the upper limit of TEM lamella heating in the irradiated area under the assumption that all excitations due to inelastic scattering of primary electrons are converted into heat. The energy uptake per unit volume and second (= adsorbed power P per unit volume V) is thus:

$$\frac{P}{V} = \frac{\Delta E W \dot{N}_e}{V}$$

where the rate of incidents electrons is given by:

$$\dot{N}_e = \frac{jA}{e}$$

Here, A denotes the illuminated area of the lamella and j the electron current density of primary electrons. In order to estimate the temperature increase due to the absorbed power, we use the Fourier law in 1D:

$$J_q = -\kappa \frac{dT}{dx} = \frac{P}{A}$$

where κ is the thermal conductivity of the manganite, J_q is the heat flux density, which is equal to the absorbed power per unit area. From these equations it follows:

$$\Delta T = \frac{L}{\kappa} \frac{P}{A}$$

where L is the length where the heat must be transported before it hits the interface to the substrate with a much higher thermal conductivity. Heat transfer due to gas convection is negligible at the used pressure range of our experiments.

For the calculation, we use a current of $I = 4$ nA on a circle of 100 nm diameter. This corresponds to an average dose rate (flux) of $r = 3.18 \times 10^4$ e/Å²s. In semiconductors, the average energy transfer per inelastic excitation $\Delta E \sim 3 E_g$, where E_g is the bandgap of the material [41]. Since the low loss excitations are the dominating feature in EELS, we use this estimate. It gives $\Delta E = 3$ eV per inelastic scattering event in PCMO.

With a measured inelastic mean free path of $\lambda = 70$ nm, the scattering probability of an electron in the thin surface regions of $t = 10$ nm is $W = t/\lambda = 0.14$. Thermal conductivity of PCMO at $T = 300$ K is $k = 1.5$ W/mK [42]. The distance of the electron irradiated surface area to the substrate is around $L = 100$ nm. This yields an upper limit of beam-induced lamella heating of $\Delta T = 15$ mK.

References

1. Kanan, M.W.; Nocera, D.G. In situ formation of an oxygen evolving catalyst in neutral water containing phosphate and Co²⁺. *Science* **2008**, *321*, 1072–1075. [[CrossRef](#)]
2. Vendelbo, S.B.; Elkjær, C.F.; Puspitasari, I.; Creemer, J.F.; Dona, P.; Mele, L.; Morana, B.; Nelissen, B.J.; van Rijn, R.; Kooyman, P.J.; et al. Visualization of oscillatory behaviour of Pt nanoparticles catalysing CO oxidation. *Nat. Mater.* **2014**, *13*, 884–890. [[CrossRef](#)]
3. Bergmann, A.; Martinez-Moreno, E.; Teschner, D.; Chernev, P.; Glied, M.; Ferreira de Araújo, J.; Reier, T.; Dau, H.; Strasser, P. Reversible amorphization and the catalytically active state of crystalline Co₃O₄ during oxygen evolution. *Nat. Commun.* **2015**, *6*, 8625. [[CrossRef](#)]
4. Arrigo, R.; Hävecker, M.; Schuster, M.E.; Ranjan, C.; Stotz, E.; Knop-Gericke, A.; Schlögl, R. In situ study of the gas-phase electrolysis of water on platinum by NAP-XPS. *Angew. Chem. Int. Ed.* **2013**, *52*, 11660–11664. [[CrossRef](#)]
5. Zheng, F.; Alayoglu, S.; Guo, J.; Pushkarev, V.; Li, Y.; Glans, P.A.; Chen, J.L.; Somorjai, G. In-situ X-ray absorption study of evolution of oxidation states and structure of cobalt in Co and CoPt bimetallic nanoparticles (4 nm) under reducing (H₂) and oxidizing (O₂) environments. *Nano Lett.* **2011**, *11*, 847–853. [[CrossRef](#)]
6. Boyes, E.D.; Gai, P.L. Environmental high resolution electron microscopy and applications to chemical science. *Ultramicroscopy* **1997**, *67*, 219–232. [[CrossRef](#)]
7. Roiban, L.; Koneti, S.; Morfin, F.; Nguyen, T.S.; Mascunan, P.; Aouine, M.; Epicier, T.; Piccolo, L. Uncovering the 3D structure of combustion-synthesized noble metal-ceria nanocatalysts. *ChemCatChem* **2017**, *9*, 4607–4613. [[CrossRef](#)]
8. Hansen, T.W.; Wagner, J.B. Environmental transmission electron microscopy in an aberration-corrected environment. *Microsc. Microanal.* **2012**, *18*, 684–690. [[CrossRef](#)]

9. Hansen, T.W.; Wagner, J.B.; Dunin-Borkowski, R.E. Aberration corrected and monochromated environmental transmission electron microscopy—Challenges and prospects. *Mater. Sci. Technol.* **2010**, *26*, 1338–1344. [[CrossRef](#)]
10. Hansen, T.W.; Wagner, J.B.; Jinschek, J.R.; Dunin-Borkowski, R.E. The titan environmental transmission electron microscope: Specifications, considerations and first results. *Microsc. Microanal.* **2009**, *15*, 714–715. [[CrossRef](#)]
11. Thermo Fisher Scientific. Available online: <https://www.fei.com/products/tem/themis-etem-for-materials-science/> (accessed on 30 August 2019).
12. Tanaka, N.; Usukura, J.; Kusunoki, M.; Saito, Y.; Sasaki, K.; Tanji, T.; Muto, S.; Arai, S. Development of an environmental high voltage electron microscope and its application to nano and bio-materials. *J. Phys. Conf. Ser.* **2014**, *522*, 012008. [[CrossRef](#)]
13. FanWu, F.; Yao, N. Advances in windowed gas cells for in-situ TEM studies. *Nano Energy* **2015**, *13*, 735–756.
14. Yokosawa, T.; Alan, T.; Pandraud, G.; Damc, B.; Zandbergen, H. In-situ TEM on (de)hydrogenation of Pd at 0.5–4.5 bar hydrogen pressure and 20–400 °C. *Ultramicroscopy* **2012**, *112*, 47–52. [[CrossRef](#)]
15. Zhang, S.; Nguyen, L.; Zhu, Y.; Zhan, S.; Tsung, C.K.; Tao, F. In-situ studies of nanocatalysis. *Acc. Chem. Res.* **2013**, *46*, 1731–1739. [[CrossRef](#)]
16. Han, B.; Stoerzinger, K.A.; Tileli, V.; Gamalski, A.D.; Stach, E.A.; Shao-Horn, Y. Nanoscale structural oscillations in perovskite oxides induced by oxygen evolution. *Nat. Mater.* **2017**, *16*, 121–126. [[CrossRef](#)]
17. Raabe, S.; Mierwaldt, D.; Ciston, J.; Uijtewaal, M.; Stein, H.; Hoffmann, J.; Zhu, Y.M.; Blochl, P.; Jooss, C. In situ electrochemical electron microscopy study of oxygen evolution activity of doped manganite perovskites. *Adv. Funct. Mater.* **2012**, *12*, 3378–3388. [[CrossRef](#)]
18. Mierwaldt, D.; Roddatis, V.; Risch, M.; Scholz, J.; Geppert, J.; Abrishami, M.E.; Jooss, C. Environmental TEM investigation of electrochemical stability of perovskite and ruddlesden-popper type manganite oxygen evolution catalysts. *Adv. Sustain. Syst.* **2017**, *1*, 1700109. [[CrossRef](#)]
19. Newcomb, S.B.; Boothroyd, C.B.; Stobbs, W.M. Specimen preparation methods for the examination of surfaces and interfaces in the transmission electron microscope. *J. Microsc.* **1985**, *140*, 195–207. [[CrossRef](#)]
20. Jacobs, J.W.M.; Verhoeven, J.F.C.M. Specimen preparation technique for high resolution transmission electron microscopy studies on model supported metal catalysts. *J. Microsc.* **1986**, *143*, 103–116. [[CrossRef](#)]
21. Giannuzzi, L.A.; Geurts, R.; Ringnalda, J. 2 keV Ga⁺ FIB milling for reducing amorphous damage in silicon. *Microsc. Microanal.* **2005**, *11*, 828–829. [[CrossRef](#)]
22. Schaffer, M.; Schaffer, B.; Ramasse, Q. Sample preparation for atomic-resolution STEM at low voltages by FIB. *Ultramicroscopy* **2012**, *114*, 62–71. [[CrossRef](#)]
23. Park, Y.C.; Park, B.C.; Romankov, S.; Park, K.J.; Yoo, J.H.; Lee, Y.B.; Yang, J.M. Use of permanent marker to deposit a protection layer against FIB damage in TEM specimen preparation. *J. Microsc.* **2014**, *255*, 180–187. [[CrossRef](#)]
24. Jesse, S.; He, Q.; Lupini, A.R.; Leonard, D.N.; Oxley, M.P.; Ovchinnikov, O.; Unocic, R.R.; Tselev, A.; Fuentes-Cabrera, M.; Sumpster, B.G.; et al. Atomic-level sculpting of crystalline oxides: Toward bulk nanofabrication with single atomic plane precision. *Small* **2015**, *11*, 5895–5900. [[CrossRef](#)]
25. Kramer, T.; Mierwaldt, D.; Scherff, M.; Kanbach, M.; Jooss, C. Developing an in situ environmental TEM set up for investigations of resistive switching mechanisms in Pt-Pr_{1-x}Ca_xMnO_{3-δ}-Pt sandwich structures. *Ultramicroscopy* **2018**, *184*, 61–70. [[CrossRef](#)]
26. Matsumoto, Y.; Sato, E. Oxygen evolution on La_{1-x}Sr_xMnO₃ electrodes in alkaline solutions. *Electrochim. Acta* **1979**, *24*, 421–423. [[CrossRef](#)]
27. Bockris, J.O.; Otagawa, T. The electrocatalysis of oxygen evolution on perovskites. *J. Electrochem. Soc.* **1984**, *131*, 290–302. [[CrossRef](#)]
28. Scholz, J.; Risch, M.; Stoerzinger, K.A.; Wartner, G.; Shao-Horn, Y.; Jooss, C. Rotating ring-disk electrode study of oxygen evolution at a perovskite surface: Correlating activity to manganese concentration. *J. Phys. Chem.* **2016**, *120*, 27746–27756. [[CrossRef](#)]
29. Sotoudeh, M.; Rajpurohit, S.; Blöchl, P.E.; Mierwaldt, D.; Norpoth, J.; Roddatis, V.; Mildner, S.; Ifland, B.; Jooss, C. Electronic structure of Pr_{1-x}Ca_xMnO₃. *Phys. Rev. B* **2017**, *95*, 235150. [[CrossRef](#)]
30. Varela, M.; Oxley, M.P.; Luo, W.; Tao, J.; Watanabe, M.; Lupini, A.R.; Pantelides, S.T.; Pennycook, S.J. Atomic-resolution imaging of oxidation states in manganites. *Phys. Rev. B* **2009**, *79*, 085117. [[CrossRef](#)]

31. De Jong, M.P.; Bergenti, I.; Dediu, V.A.; Fahlman, M.; Marsi, M.; Taliani, C. Evidence for Mn^{2+} ions at surfaces of $La_{0.7}Sr_{0.3}MnO_3$ thin films. *Phys. Rev. B* **2005**, *71*, 014434. [[CrossRef](#)]
32. Bugnet, M.; Overbury, S.H.; Wu, Z.L.; Epicier, T. Direct visualization and control of atomic mobility at {100} surfaces of ceria in the environmental transmission electron microscope. *Nano Lett.* **2017**, *17*, 7652–7658. [[CrossRef](#)]
33. Rudawski, N.G.; Jones, K.S.; Morarka, S.; Law, M.E.; Elliman, R.G. Stressed multidirectional solid-phase epitaxial growth of Si. *J. Appl. Phys.* **2009**, *105*, 081101. [[CrossRef](#)]
34. Evans, P.G.; Chen, Y.; Tilka, J.A.; Babcock, S.E.; Kuech, T.F. Crystallization of amorphous complex oxides: New geometries and new compositions via solid phase epitaxy. *Curr. Opin. Solid State Mater. Sci.* **2018**, *22*, 229–242. [[CrossRef](#)]
35. Mildner, S.; Beleggia, M.; Mierwaldt, D.; Hansen, T.W.; Wagner, J.B.; Yazdi, S.; Kasama, T.; Ciston, J.; Zhu, Y.; Jooss, C. Environmental TEM study of electron beam induced electrochemistry of $Pr_{0.64}Ca_{0.36}MnO_3$ catalysts for oxygen evolution. *J. Phys. Chem. C* **2015**, *119*, 5301–5310. [[CrossRef](#)]
36. Egerton, R.F.; Li, P.; Malac, M. Radiation damage in the TEM and SEM. *Micron* **2004**, *35*, 399–409. [[CrossRef](#)]
37. Gonzalez, E.; Abreu, Y.; Cruz, C.M.; Piñera, I.; Leyva, A. Molecular-dynamics simulation of threshold displacement energies in $BaTiO_3$. *Nucl. Instrum. Methods Phys. Res. B* **2015**, *358*, 142–145. [[CrossRef](#)]
38. Giannuzzi, L.A.; Stevie, F.A. A review of focused ion beam milling techniques for TEM specimen preparation. *Micron* **1999**, *30*, 197–204. [[CrossRef](#)]
39. Momma, K.; Izumi, F. VESTA 3 for three-dimensional visualization of crystal, volumetric and morphology data. *J. Appl. Crystallogr.* **2011**, *44*, 1272–1276. [[CrossRef](#)]
40. Koch, C.T. Determination of Core Structure Periodicity and Point Defect Along Dislocations. Ph.D. Thesis, Arizona State University, Tempe, AZ, USA, May 2002.
41. Klein, C.A. Bandgap dependence and related features of radiation ionization energies in semiconductors. *J. Appl. Phys.* **1968**, *39*, 2029–2038. [[CrossRef](#)]
42. Thiessen, P.; Roddatis, V.; Rieger, F.; Belenchuk, A.; Keunecke, M.; Moshnyaga, V.; Jooss, C. Effect of charge ordering on cross-plane thermal conductivity in correlated perovskite oxide superlattices. *Phys. Rev. B* **2018**, *98*, 195114. [[CrossRef](#)]



© 2019 by the authors. Licensee MDPI, Basel, Switzerland. This article is an open access article distributed under the terms and conditions of the Creative Commons Attribution (CC BY) license (<http://creativecommons.org/licenses/by/4.0/>).